Airborne SAR Moving Target Signatures and Imagery Based on LVD

Yang, Lei; Bi, Guoan; Xing, Mengdao; Zhang, Liren

2015

Yang, L., Bi, G., Xing, M., & Zhang, L. (2015). Airborne SAR Moving Target Signatures and Imagery Based on LVD. IEEE Transactions on Geoscience and Remote Sensing, 53(11), 5958-5971.

https://hdl.handle.net/10356/81593

https://doi.org/10.1109/TGRS.2015.2429678

Airborne SAR Moving Target Signatures and Imagery Based on LVD

Lei Yang, *Member, IEEE,* Guoan Bi, *Senior Member, IEEE*, Mengdao Xing, *Member, IEEE,* and Liren Zhang, *Senior Member, IEEE*

Abstract: This paper presents a new ground moving target imaging (GMTIm) algorithm for airborne synthetic aperture radar (SAR), based on a novel time-frequency representation (TFR), Lv's distribution (LVD). We first analyze generic moving target signatures for a multichannel SAR, and then derive the analytical spectrum of a point target moving at a constant velocity by polar format algorithm for SAR image formation. SAR motion deviation from predetermined flight track is considered to facilitate airborne SAR applications. LVD, as a recently developed TFR for analysis of multicomponent linear frequency modulated (LFM) signal, is adopted to represent the target kinematic spectrum in Doppler centroid frequency and chirp rate domain. As a result, the proposed SAR-GMTIm algorithm is capable of imaging multiple moving targets even when they are located at the same range resolution cell. Some practical issues such as imaging maneuvering targets and small/weak targets are discussed to enhance the applicability of the proposed algorithm. Simulation results with isotropic point moving targets are presented to validate the effectiveness and superiority of the proposed algorithm. Raw data collected by an airborne multichannel SAR is also used to verify the performance improvement made by the proposed algorithm.

Index Terms — Synthetic aperture radar (SAR), ground moving target imaging (GMTIm), time-frequency representation (TFR), Lv's distribution (LVD).

I. INTRODUCTION

Synthetic aperture radar (SAR) for ground moving target imaging (GMTIm) has been gaining increasing interest in SAR community [1]-[4]. Since the SAR-GMTIm has the capability of geo-location and image-formation of a moving target, it has great potentials in both civilian and military applications [5]-[6]. Generally, the SAR sensor is mounted on an airborne platform flying along a predetermined track to

L. Yang and G. Bi are with Division of Information Engineering, School of Electrical and Electronic Engineering, Nanyang Technological University, Singapore, 639798. (Email: yanglei@ntu.edu.sg, and egbi@ntu.edu.sg); M. Xing is with National Key Lab of Radar Signal Processing, Xidian University, Xi'an, China, 710071; and L. Zhang is with UAE University (Email: lzhang@uaeu.ac.ae).

generate a so-called synthetic aperture, during which the radar transmits a large number of broadband pulses at a fixed pulse repetition interval (PRI). When the SAR sensor observes a ground terrain with moving targets, it receives the reflected pulses containing the echoes from both the moving targets and the stationary terrain which is commonly referred to clutter. SAR image formation process, which is conventionally designed for stationary terrain imaging, cannot accurately match the unknown target movement. This will result in both displacement and smearing in the SAR moving target image [1]-[2].

The intended SAR-GMTIm algorithm allows the generation of a spatial moving target image against the clutter. Various approaches have been investigated by a single-channel SAR [7]-[12]. However, these approaches are highly dependent on the target signal-to-clutter-noise ratio (SCNR) in the echo signal. To mitigate the clutter, SAR equipped with multiple channels in along-track configuration is widely employed [2], [13]-[14]. Kinds of effective methods to filter the moving target signature from the clutter have been proposed, such as displaced phase center antenna (DPCA) [15] and space-time adaptive processing (STAP) [16]. STAP is an adaptive filter that is optimal to be combined with multichannel SAR in terms of moving targets' SCNR maximization [2], [16]. DPCA is often considered as a simplified version of STAP, which requires low computational load, and it is easy to implement [6], [16].

For 2-D SAR echo signal of range frequency and azimuth (slow) time, the coupling between the range frequency and radar-target range variation is known as the target range migration, which can be used to characterize the target signature during the coherent processing interval (CPI). A common practice is that the target range migration is approximated by Taylor series up to second order [7]-[10]. Higher order terms would be considered in high-resolution SAR applications and/or highly maneuvering target scenario. Conventionally, Keystone transformation (KT), first introduced in [7], is a useful tool to compensate the range walk that is the linear component of the range migration. Due to its capability to eliminate an arbitrary range walk without kinetic information about the moving target [8], KT has been widely used for SAR moving target imaging [5]-[6]. Furthermore, the original KT is extended to the second order version that can correct the range curvature or the quadratic component of the range migration [9]-[10].

Once the target range migration is corrected, the target can be focused in range dimension by range compression. Prior to azimuth compression, the azimuth phase modulation (APM) should be compensated

or match-filtered for achieving a fully focused target image. Considering that the APM shows a linear frequency modulated (LFM) form, time-frequency (TF) analysis is a suitable tool [17]-[21]. Wigner-Ville distribution (WVD) [17] is a well-known method for the TF representation (TFR). However, it is important to be aware that there may be multiple moving targets located closely in the same range cell. In such a case, the APM should be in a multicomponent LFM form, and the WVD would be no longer useful due to its bi-linearity causing cross-terms [18]-[19]. To mitigate the cross-terms, Radon [18] and Hough [19] transforms are utilized to concentrate the target energy within a small area on a corresponding parametric plane. Radon-Wigner transform (RWT) [18], Wigner-Hough transform (WHT) [19] and Radon-Ambiguity transform (RAT) [20] are three typical methods. However, these methods are still bilinear and cannot be recognized as true representations for the physical attributes of the LFM signal, i.e., centroid frequency and chirp rate. This is because rotational and searching operations in the TF plane are required during the implementation [22]. Another popular TFR is the linear fractional Fourier transform (FrFT) [21], which is free of cross-terms. Again, the FrFT cannot provide a true representation of centroid frequency and chirp rate [22].

In this paper, a novel TFR, known as Lv's distribution (LVD), is introduced to represent multiple moving targets in a Doppler centroid frequency and chirp rate (CFCR) domain. Different from other reported methods, LVD is a true and natural TFR because it is free of rotational and searching operations and without introducing any non-physical attributes such as rotation angle or order [22]. Since LVD provides superior performance in dealing with multicomponent LFM signal [22], our intended SAR-GMTIm algorithm is capable of imaging multiple moving targets even when they are closely located.

As an accurate characterization of moving target signature is critical for the target imagery, in this paper, we analyze the target signature before introducing the intended SAR-GMTIm algorithm. Different from the analysis reported in [2], we derive the moving target signature that is convenient for TF analysis. In [2], a match-filter bank based on a grid of target motion hypotheses is required to cover the target truth to image a potential moving target. However, this strategy may be intractable for imaging multiple moving targets. Therefore, the main contribution of this paper is that a uniform framework is proposed by integrating the analysis of SAR moving target signature with the imagery of multiple moving targets based on the LVD

representation. Further detailed analysis of SAR image formation process gives an analytical target spectrum in range-Doppler domain. The polar format algorithm (PFA) [23]-[24] is adopted for this process, as it inherently has the same mechanism as KT. As such, it is capable of simultaneously correcting the range walk of stationary clutter and multiple moving targets. For airborne SAR applications, the uncompensated SAR motion error is also considered, and the error signature is presented. Some practical issues for imaging maneuvering targets and small/weak targets are also discussed. Finally, both point target simulation and raw SAR data experiment are presented for the verification of the proposed algorithm.

The remainder of this paper is organized as follows. Section II analyzes moving target signatures for airborne multichannel SAR. Section III further derives the moving target spectrum using PFA. Section IV introduces LVD for the representation of multiple moving targets and proposes our intended SAR-GMTIm algorithm based on the LVD representation. Section V discusses several practical issues to enhance applicability of the proposed algorithm. Section VI presents the processing results of both the point target simulation and raw SAR data experiment. Finally, conclusions are drawn in Section VII.

II. AIRBORNE SAR MOVING TARGET SIGNATURES

In this section, a generic radar-target geometry is first presented, and then the signal model of either a stationary scatterer or ground target moving at a constant velocity is established. Following common practice, the SAR sensor is modeled as a linear system such that the radar echo signal represents the linear superposition of the echoes from moving targets and stationary scatterers. Moreover, both the moving targets and stationary scatterers are assumed to be isotropic point-like targets. Therefore, our intended algorithm would mainly focus on medium and low resolution SAR applications, where a truck-size moving target can be approximately modeled as an isotropic point target. Far-field hypothesis and narrow-beam assumption are adopted in our intended signal model.

A. Radar-Target Geometry

Consider Fig. 1 that depicts the geometry of airborne SAR and ground targets. In ideal case, the airborne SAR flies along a predetermined track with a constant velocity $\mathbf{v}$ at a height H. We establish a spatial Cartesian coordinate system as XYZ-O, where X axis is the ideal radar flight track, Y axis is parallel to the

ground plane, and Z axis is determined by the right hand rule. The origin of the coordinate system, O , is set at broadside position with respect to the observing scene center O' . Define $\mathbf{R}_0 = \mathrm{O}' - \mathrm{O}$ giving the nearest range vector from the radar flight track to the scene center.

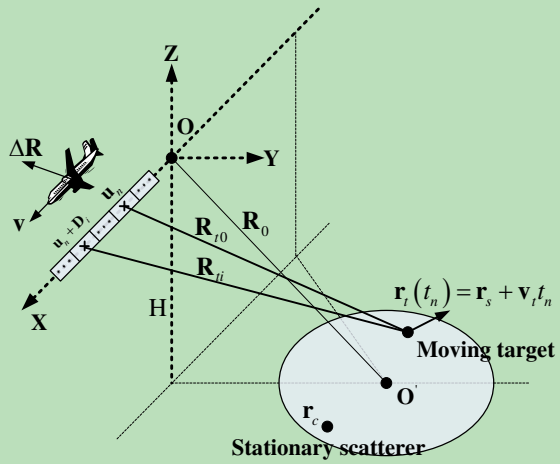

Fig. 1. Radar-target geometry.

A linear array of radar antenna along the flight track is employed for multichannel SAR. In Fig. 1, the airborne side-looking SAR's position is represented by the reference position vector $\mathbf{u}_n = \mathbf{v} \cdot t_n$ for the phase center of the linear antenna array, where t_n indicates the slow-time of the radar pulse repetition within CPI, $[-T_a/2, T_a/2]$. Consider a single radar transmitter locating at this reference position and multiple receivers along the linear array with I receiving elements. The i -th receiving element is given at the position $\mathbf{u}_n + \mathbf{D}_i$, where $\mathbf{D}_i = \mathrm{D}_i \cdot \bar{\mathbf{x}}$ and $\bar{\mathbf{x}}$ is the unit vector of X axis and D_i is the spacing between the antenna reference position and the i -th receiving element. To incorporate ground target, in Fig. 1, $\mathbf{r}_c$ is generally used to denote stationary scatterers within the observing scene, and the moving target is represented by its rectilinear trajectory $\mathbf{r}_t(t_n) = \mathbf{r}_s + \mathbf{v}_t t_n$, where $\mathbf{v}_t$ is the target velocity and $\mathbf{r}_s$ is the target position at t_n=0. Furthermore, $\mathbf{r}_s = \mathbf{R}_0 + \mathbf{r}_0$ where $\mathbf{r}_0$ denotes the target offset from the scene center. At this point, the moving target ranges from the radar transmitter and i -th receiver can be given as (Fig. 1)

$$\mathbf{R}_{t0}(t_n) = \mathbf{r}_t(t_n) - \mathbf{u}_n \quad \text{and} \quad \mathbf{R}_{ti}(t_n) = \mathbf{R}_{t0}(t_n) - \mathbf{D}_i \ , \tag{1}$$

respectively. In the above analysis, the range from the radar to the moving target is formulated under the assumption that the airborne SAR flies ideally along the predetermined track. However, due to inevitable atmosphere turbulence and insufficient accuracy of navigation measurement, the actual flight track may deviate from the expected path [25]-[27]. To facilitate the formulation in (1) for actual airborne SAR applications, the uncompensated SAR motion deviation, denoted as a position error $\Delta\mathbf{R} = \Delta\mathbf{R}(t_n)$ in Fig. 1, should be taken into account as

$$\tilde{\mathbf{R}}_{t0}(t_n) = \mathbf{R}_{t0}(t_n) - \Delta\mathbf{R}(t_n) \quad \text{and} \quad \tilde{\mathbf{R}}_{ti}(t_n) = \tilde{\mathbf{R}}_{t0}(t_n) - \mathbf{D}_i \ . \tag{2}$$

B. SAR Moving Target Signal Model

Assuming the radar pulse with bandwidth B about carrier frequency f_0 is transmitted at the single transmitter, the echo signal backscatterered from the moving target $\mathbf{r}_t = \mathbf{r}_t(t_n)$ and received by the i -th receiving element can be shown as

$$s_i(\hat{t}, t_n; \mathbf{r}_t) = b_R \cdot p_r\left(\hat{t} - \frac{R_i(t_n;\mathbf{r}_t)}{\mathrm{c}}\right)\exp\left[j2\pi f_0\left(\hat{t} - \frac{R_i(t_n;\mathbf{r}_t)}{\mathrm{c}}\right)\right] \tag{3}$$

where b_R represents amplitude modulation during the radar signal propagation. Notwithstanding the fact that this amplitude modulation may fluctuate in realistic environment [2], it is treated as a constant value here as this assumption will hardly affect our intended result. In (3), $p_r(\cdot)$ denotes the baseband waveform of the transmitted pulse, c is the speed of light, and $\hat{t}$ is used to mark the 'fast-time' for measuring the time-delay due to the signal propagation in line with the two-way target slant range

$$R_i(t_n;\mathbf{r}_t) = \left\|\tilde{\mathbf{R}}_{t0}(t_n)\right\| + \left\|\tilde{\mathbf{R}}_{ti}(t_n)\right\| \tag{4}$$

where $\|\cdot\|$ denotes Euclidean norm operator, and $\left\|\tilde{\mathbf{R}}_{t0}(t_n)\right\|$ and $\left\|\tilde{\mathbf{R}}_{ti}(t_n)\right\|$ are the moving target slant ranges from the transmitter and i -th receiver, respectively. Defining $P_r(\cdot)$ to be the normalized baseband spectrum, (3) can be transformed into the target spectrum representation as

$$S_i(f,t_n;\mathbf{r}_t)=\frac{b_R}{B}\cdot\left|P_r(f-f_0)\right|^2\exp\left[-j\frac{2\pi f}{\mathrm{c}}R_i(t_n;\mathbf{r}_t)\right] \tag{5}$$

where $|\cdot|$ denotes the absolute value (or modulus) operator, and $f=f_0+\Delta f$, $\Delta f\in[-B/2,B/2]$.

From the derivations in (3)-(5), it is noticed that the target echo signal received by the i-th receiving element is the radar pulse propagated from the transmitter at $\mathbf{u}_n$ to the moving target at $\mathbf{r}_t$ and backscatterered to the i-th receiving element at $\mathbf{u}_n+\mathbf{D}_i$. Thus, strictly speaking, the target slant range given in (4) is bistatic. Based on a commonly used assumption that if the nearest range $\mathrm{R}_0=\|\mathbf{R}_0\|$ is much larger than the element displacement D_i, the bistatic target range can be approximately replaced by an equivalent range of round-trip propagation between the target and a monostatic antenna with its virtual phase center at $\mathbf{u}_n+\mathbf{d}_i$ [2], where $\mathbf{d}_i=d_i\cdot\bar{\mathbf{x}}$ and $d_i=D_i/2$. Then, (4) can be rewritten as

$$R_i(t_n;\mathbf{r}_t)\approx 2\left\|\tilde{\mathbf{R}}_{t0}(t_n)-\mathbf{d}_i\right\| . \tag{6}$$

Therefore, the multiple SAR channels correspond to the multiple virtual elements $\mathbf{u}_n+\mathbf{d}_i$ in the equivalently monostatic configuration. For d_i =0, it corresponds to the reference channel.

By substituting (1) and (2) into (6), the target range can be further approximated as

$$R_i(t_n;\mathbf{r}_t)=2\left\|\mathbf{r}_t(t_n)-\mathbf{u}_n-\mathbf{d}_i-\Delta\mathbf{R}(t_n)\right\|\approx 2\left[\left\|\mathbf{r}_t(t_n)-\mathbf{u}_n-\mathbf{d}_i\right\|-\Delta R(t_n)\right] \tag{7}$$

where $\Delta R(t_n)$ denotes the projection of $\Delta\mathbf{R}(t_n)$ in slant range direction. The approximation in (7) holds under the condition that the slant range error $\Delta R(t_n)$ is considered [26].

Given $\|\mathbf{R}_0-\mathbf{u}_n\|$, which is known as the reference range from the SAR reference channel to the scene center, is much larger than the extent of the observing scene, one convenient approximation, that is Taylor series expansion up to the second order, may simplify the far-field target range in (7) as

$$R_i(t_n;\mathbf{r}_t)\approx 2\left[\xi_0+\boldsymbol{\xi}_1\mathbf{r}_0+\frac{1}{2}\xi_2\|\mathbf{r}_0\|^2+R_{d_i}+(\boldsymbol{\xi}_1+\xi_2\mathbf{r}_0)\mathbf{v}_t t_n+\frac{1}{2}\xi_2\mathbf{v}_t{}^2 t_n{}^2\right]-2\Delta R(t_n) \tag{8}$$

where $R_{d_i} = -\left(\xi_1 + \xi_2 \mathbf{r}_0 + \xi_2 \mathbf{v}_t t_n\right)\mathbf{d}_i + \frac{1}{2}\xi_2 \left\|\mathbf{d}_i\right\|^2$ includes all the terms corresponding to $\mathbf{d}_i$, and $\xi_0 = \left\|\mathbf{R}_0 - \mathbf{u}_n\right\|$, $\xi_1 = \left(\mathbf{R}_0 - \mathbf{u}_n\right)/\left\|\mathbf{R}_0 - \mathbf{u}_n\right\|$ and $\xi_2 = 1/\left\|\mathbf{R}_0 - \mathbf{u}_n\right\|$ refer to the constant, linear and quadratic Taylor series coefficients, respectively. Substituting (8) into (5), the moving target spectrum can be expressed as

$$S_i\left(k, t_n; \mathbf{r}_t\right) \approx \frac{b_R}{B} \exp\left[j\Psi_i\left(k; t_n\right)\right] \quad \text{where}$$
$$\Psi_i\left(k; t_n\right) = -k\xi_0 - k\xi_1 \mathbf{r}_0 - \frac{1}{2}k\xi_2 \left\|\mathbf{r}_0\right\|^2 - k R_{d_i} - k\left(\xi_1 + \xi_2 \mathbf{r}_0\right)\mathbf{v}_t t_n - \frac{1}{2}k\xi_2 \mathbf{v}_t^{\,2} t_n^{\,2} + k\Delta R\left(t_n\right) \quad . \qquad (9)$$

In (9), $k = 4\pi f / \mathrm{c}$ is the wavenumber variable. At this point, we have concluded a generalized target signal model in multichannel SAR as the phase equation in (9), where the SAR moving target signatures can be summarized as follows. The first three terms in the phase component of (9) can be interpreted as the target location signature, since they are independent of the target movement. The phase term, $-k R_{d_i}$ in (9), for the specified i-th channel lumps together all the phases that are different from the reference channel. The next two phase terms in (9), which are characterized by linear and quadratic modulations of target motion vector $\mathbf{v}_t t_n$, are known as the target kinematic signature. The last phase term, resulting from the slant range error $\Delta R\left(t_n\right)$, is known as the error signature. With the above moving target signatures, we will further analyze the moving target spectral signatures that are important to obtain a focused moving target image.

III. MOVING TARGET SPECTRAL SIGNATURES

As noted in (9), the range wavenumber k and azimuth slow-time t_n or equivalently spatial sample variable $\mathbf{u}_n$ are coupled with each other in each phase term. This coupling, known as the range migration, is the underlying mechanism resulting in SAR image degradation. Generally, a SAR image formation process is designated to remove the coupling or correct the range migration, and an explicit target spectrum can be obtained after this process. Many mature techniques [23] have been developed for the SAR image formation of stationary terrain. In this paper, we adopt the polar format algorithm (PFA) [23]-[24] for the SAR image formation process. To accommodate SAR imagery on slant range plane, let us consider some equivalence that will be used for our subsequent development,

$$\mathbf{r}_0 = x\bar{\mathbf{x}} + r\bar{\mathbf{r}}, \quad \mathbf{R}_0 = \mathrm{R}_0\bar{\mathbf{r}}, \quad \mathbf{v}_t = v_x\bar{\mathbf{x}} + v_r\bar{\mathbf{r}}, \quad \mathbf{u}_n = u_n\bar{\mathbf{x}} \ , \tag{10}$$

where $\bar{\mathbf{r}}$ denotes the unit vector of the slant-range, and x and r are the target positions in azimuth and slant-range, respectively, and v_x and v_r are the target along-track and cross-track (radial) velocities, respectively.

The first phase term in (9) can be simply compensated by multiplying an exponential term $\exp\left(jk\sqrt{u_n^{\,2} + \mathrm{R}_0^{\,2}}\right)$ for a dechirping operation [23], [27]. Next, according to PFA, which relies on the assumption of planar wavefront propagation, the range curvature phase term $-k\xi_2\|\mathbf{r}_0\|^2/2$ in (9) could be negligible. Under this assumption, the maximum size of the focused SAR image will be limited upon $2\rho_x\sqrt{2\mathrm{R}_0/\lambda}$ in diameter, where ρ_x is the required azimuth resolution. To form an extended SAR image in high resolution, advanced PFA can be adopted with the correction of the range curvature [23], [27].

It is well-known that the SAR phase data are represented in polar format in Fourier spectrum domain [24]. PFA is such a process that reformats the data samples from the polar grid into a Cartesian grid. As such, the coupling between the range frequency and azimuth slow-time can be removed, and then Fourier transform (FT) can be applied to form a SAR image. In practice, two tandem resampling operations, named range and azimuth resampling, are applied to resample the data from the polar grid into a Keystone grid first which is then resampled into the Cartesian (rectangular) grid. From (9) and (10), the SAR phase data of the i -th channel in polar format can be explicitly written as

$$\begin{aligned}\Psi_i^{\mathrm{POL}}(k;t_n) = &-k\frac{-u_n}{\sqrt{u_n^{\,2} + \mathrm{R}_0^{\,2}}}x - k\frac{\mathrm{R}_0}{\sqrt{u_n^{\,2} + \mathrm{R}_0^{\,2}}}r + \Psi_{d_i} \\ &-k\frac{(x-u_n)v_x + (r+\mathrm{R}_0)v_r}{\sqrt{u_n^{\,2} + \mathrm{R}_0^{\,2}}}t_n - k\frac{v_x^{\,2} + v_r^{\,2}}{2\sqrt{u_n^{\,2} + \mathrm{R}_0^{\,2}}}t_n^{\,2} + k\Delta R(t_n)\end{aligned} \tag{11}$$

where

$$\Psi_{d_i} = -kR_{d_i} = k\left(\frac{-u_n}{\sqrt{u_n^{\,2} + \mathrm{R}_0^{\,2}}}d_i + \frac{x}{\sqrt{u_n^{\,2} + \mathrm{R}_0^{\,2}}}d_i + \frac{v_x t_n}{\sqrt{u_n^{\,2} + \mathrm{R}_0^{\,2}}}d_i - \frac{d_i^{\,2}}{2\sqrt{u_n^{\,2} + \mathrm{R}_0^{\,2}}}\right) . \tag{12}$$

Defining the synthetic aperture angle θ_n, and $\cos\theta_n = \mathrm{R}_0 \big/ \sqrt{u_n^{\,2} + \mathrm{R}_0^{\,2}}$ and $\sin\theta_n = -u_n \big/ \sqrt{u_n^{\,2} + \mathrm{R}_0^{\,2}}$, the polar grid can be given as the coordinates (k, θ_n). In PFA, the range resampling is first performed in radial direction as the kernel $k_r = k\cos\theta_n$ [24], where k_r is the resampled range wavenumber. The range resampling is to remove the dependence of k_r on θ_n. After the range resampling, the phase data in (11) can be written in the Keystone grid (k_r, θ_n) as

$$\begin{aligned}\Psi_i^{\mathrm{KEY}}(k_r; t_n) \approx & -k_r \frac{-u_n}{\mathrm{R}_0} x - k_r r + \Psi_{d_i} \\ & - k_r \frac{-u_n v_x + (r + \mathrm{R}_0) v_r}{\mathrm{R}_0} t_n - k_r \frac{v_x^{\,2} + v_r^{\,2}}{2\mathrm{R}_0} t_n^{\,2} + k_r \Delta R(t_n)\end{aligned} \tag{13}$$

where $\Psi_{d_i} = k_r \left(\frac{-u_n}{\mathrm{R}_0} d_i + \frac{x}{\mathrm{R}_0} d_i + \frac{v_x t_n}{\mathrm{R}_0} d_i - \frac{d_i^{\,2}}{2\mathrm{R}_0} \right)$. The assumption of small θ_n is used for the approximation in (13). From $f = f_0 + \Delta f$, we have $k = k_0 + \Delta k$, where $k_0 = 4\pi f_0 / \mathrm{c}$ is the wavenumber centroid and $\Delta k = 4\pi \Delta f / \mathrm{c}$. Similarly, we have $k_r = k_0 + \Delta k_r$, where $k_r = 4\pi f_r / \mathrm{c}$ and $\Delta k_r = 4\pi \Delta f_r / \mathrm{c}$, and $f_r = f_0 + \Delta f_r$.

For the next step, the azimuth resampling operates as $k_x = k_r \tan\theta_n = -k_r u_n / \mathrm{R}_0$, where k_x indicates the azimuth wavenumber, and the Cartesian coordinates are (k_r, k_x). The azimuth resampling is aimed at removing the dependence of $k_x = -k_r u_n / \mathrm{R}_0$ on k_r. By setting $k_r = k_0$, the azimuth wavenumber can also be written as $k_x = -k_0 \tilde{u}_n / \mathrm{R}_0$, where $\tilde{u}_n$ is introduced to denote the azimuth resampled data positions to cope with the azimuth resampling. Two outcomes can be therefore highlighted as $k_r u_n = k_0 \tilde{u}_n$ and $k_r t_n = k_0 \tilde{t}_n$, where $\tilde{t}_n$ is the resampled slow-time that is the temporal sampling variable proportional to the spatial variable $\tilde{u}_n = v\tilde{t}_n$ and $v = \|\mathbf{v}\|$. Then, the phase data in the Cartesian coordinates can be given as

$$\begin{aligned}\Psi_i^{\mathrm{RECT}}(k_r; k_x) = & -k_x x - k_r r + \Psi_{d_i} \\ & - k_x v_x \frac{k_0}{k_r} \tilde{t}_n - k_0 \frac{(r + \mathrm{R}_0) v_r}{\mathrm{R}_0} \tilde{t}_n - k_0^{\,2} \frac{1}{k_r} \frac{v_x^{\,2} + v_r^{\,2}}{2\mathrm{R}_0} \tilde{t}_n^{\,2} + k_r \Delta R\left(-\frac{k_x}{k_r} \frac{\mathrm{R}_0}{v} \right)\end{aligned} \tag{14}$$

where $\Psi_{d_i} = k_x d_i + k_r \frac{x}{\mathrm{R}_0} d_i + k_0 \frac{v_x \tilde{t}_n}{\mathrm{R}_0} d_i - k_r \frac{d_i^{\,2}}{2\mathrm{R}_0}$.

In (14), $k_r \Delta R\left(-k_x \mathrm{R}_0 / k_r v\right)$ is the phase term related to the uncompensated SAR motion error, which will be discussed in Section V.A. Using the expansion $\frac{1}{k_r} = \frac{1}{k_0 + \Delta k_r} \approx \frac{1}{k_0} - \frac{1}{k_0^{\,2}} \Delta k_r$, (14) can be approximated as

$$\Psi_i^{\mathrm{RECT}}\left(k_r; k_x\right) \approx -k_x x - k_r r + \Psi_{d_i} - k_0 \frac{\left(r + \mathrm{R}_0\right) v_r}{\mathrm{R}_0} \tilde{t}_n - k_0 \frac{\left(v - v_x\right)^2 + v_r^{\,2}}{2\mathrm{R}_0} \tilde{t}_n^{\,2} + k_0 \frac{v^2}{2\mathrm{R}_0} \tilde{t}_n^{\,2} \tag{15}$$

where $\Psi_{d_i} = k_x \frac{v - v_x}{v} d_i + k_r \frac{2x - d_i}{2\mathrm{R}_0} d_i$. The range curvature phase terms are ignored in (15). This would be only feasible for slow moving target with constant velocity. For highly maneuvering target, especially in high-resolution SAR applications, the target range curvature or even high-order range cell migration (RCM) should be taken into account. Therefore, a dedicated operation of RCM correction (RCMC) should be included in the SAR-GMTIm processing chain which will be involved in Section IV.C.

In (15), a generalized target spectrum is given for each SAR channel, where the resampled range wavenumber k_r is no longer coupled with the azimuth variables k_x, $\tilde{u}_n$ or $\tilde{t}_n$. The first two terms in (15) show the Fourier form of the true target location in azimuth and slant-range, respectively. Applying FT operations to the azimuth and range wavenumber, k_x and k_r, respectively, the target can be focused at (x, r). However, due to the target movement, additional APM can be found as the last three terms in (15), which will make the target both displaced and defocused in the SAR image.

As seen from the above image formation process, although PFA is originally designed for stationary terrain imaging, it can also remove the coupling for moving targets. When we refer to the highlighted outcome $k_r t_n = k_0 \tilde{t}_n$ or $\left(k_0 + \Delta k_r\right) t_n = k_0 \tilde{t}_n$, it is noted that the azimuth resampling in PFA is identical to the well-known KT interpolator $\left(f_0 + \Delta f_r\right) t_n = f_0 \tilde{t}_n$ as given in [7]-[8]. This reveals that for the azimuth resampling in PFA, it has the same mechanism as KT, which explains PFA has the capability to correct the range walk of stationary clutter and moving target, simultaneously. Strictly speaking, the moving targets should move within the range resolution cell. The case that the target's movement exceeds the range cell will be discussed in Section V.B. Therefore, PFA is a good choice for SAR image formation of both stationary clutter and moving targets, where the stationary clutter can be imaged with fully focused

response, and the range walk of the moving target can be corrected though its response may still be displaced and defocused in azimuth dimension.

To enhance the moving target's SCNR, DPCA is employed for the clutter suppression [13]-[14]. Two echo signals received by the i-th and reference channel are assumed to have a similar SAR geometry that is only separated by a time shift d_i/v. The clutter suppressed signal can be easily generated by subtracting the signal of the reference channel from the time-shifted signal of the i-th channel. Thus, the clutter-suppressed target spectrum in post-PFA data domain yields

$$\begin{aligned} S\left(k_r;k_x\right) &= S_i\left(k_r;k_x,\tilde{t}_n-\frac{d_i}{v}\right)-S_0\left(k_r;k_x\right) \\ &= \frac{b_R}{B}\cdot 2j\sin\left(\Psi_{\text{in}}/2\right)\exp\left(j\Psi_{\text{in}}/2\right)\exp\left[j\Psi_0^{\text{RECT}}\left(k_r;k_x\right)\right] \end{aligned} \tag{16}$$

where $S_0\left(k_r;k_x\right)$ is the target spectrum of the reference channel, and $S_i\left(k_r;k_x,\tilde{t}_n-d_i/v\right)$ is the time-shifted target spectrum of the i-th channel. It is important to be aware that the good performance of DPCA depends on the multiple channels being properly balanced in terms of frequency response and beam pattern [13]. In addition, Ψ_{in} in (16) is known as the interferometric phase [13]-[14] which is computed as

$$\Psi_{\text{in}}=\Psi_i^{\text{RECT}}\left(k_0;k_x,\tilde{t}_n-\frac{d_i}{v}\right)-\Psi_0^{\text{RECT}}\left(k_0;k_x\right)\approx k_0\frac{d_i^2}{2\text{R}_0}+k_0\frac{\left(r+R_0\right)v_r}{R_0}\frac{d_i}{v}\ . \tag{17}$$

By substituting (15) into (16), the clutter-suppressed moving target spectrum in post-PFA data domain can be rewritten as

$$S\left(k_r;k_x\right)\approx A\cdot\exp\left[-jk_xx-jk_rr-jk_0\frac{\left(r+\text{R}_0\right)v_r}{\text{R}_0}\tilde{t}_n-jk_0\frac{\left(v-v_x\right)^2+v_r^2}{2\text{R}_0}\tilde{t}_n^{\,2}+jk_0\frac{v^2}{2\text{R}_0}\tilde{t}_n^{\,2}\right] \tag{18}$$

where $A=2jb_R\sin\left[\Psi_{\text{in}}/2\right]\exp\left[j\Psi_{\text{in}}/2\right]/B$ is the complex amplitude.

IV. MOVING TARGET IMAGERY BASED ON LVD

As noted in (18), due to the target movement, additional APM can be observed as the last three phase terms in linear and quadratic modulations. Because of the APM, moving target will be both displaced and

defocused in the SAR image. To achieve a focused moving target image, in this section, the novel LVD is applied to represent the APM in Doppler CFCR domain.

A. LFM Signal Model

From (18), the moving target can be focused in range dimension by simply using a FT with respect to k_r. Then, substituting $k_x = -k_0 v\tilde{t}_n / \mathrm{R}_0$ and $k_0 = 4\pi/\lambda$, the azimuth phase modulated signal in range-compressed data domain can be shown with the single variable $\tilde{t}_n$ as

$$s(\tilde{t}_n) = A \cdot \exp\left[j2\pi\left(f^{dc} - f^{dt}\right)\tilde{t}_n + j\pi\left(\gamma^{dc} - \gamma^{dt}\right)\tilde{t}_n^{\,2}\right] \tag{19}$$

where

$$f^{dc} = \frac{2xv}{\lambda \mathrm{R}_0}, \quad f^{dt} = \frac{2(r+\mathrm{R}_0)v_r}{\lambda \mathrm{R}_0}, \quad \gamma^{dc} = \frac{2v^2}{\lambda \mathrm{R}_0}, \quad \gamma^{dt} = \frac{2(v-v_x)^2 + 2v_r^{\,2}}{\lambda \mathrm{R}_0} \ . \tag{20}$$

It can be seen from (19) that the 1-D azimuth signal is modeled as a LFM form. The linear modulated parameter $f^d = f^{dc} - f^{dt}$ is known as the Doppler centroid frequency, where f^{dc} is the necessary frequency determined by the target location x, and f^{dt} is a frequency shift due to the target radial velocity v_r, which consequently results in the moving target displacement in SAR image. The quadratic modulated parameter $\gamma^d = \gamma^{dc} - \gamma^{dt}$ corresponds to the Doppler chirp rate, where γ^{dc} is the common chirp rate for both clutter and moving target, and γ^{dt} is a chirp rate difference mainly due to the target along-track velocity v_x, which in turn results in moving target defocusing.

B. LVD For SAR Moving Target Representation

In (19), only one moving target is considered, and the target signal model contains only one LFM component. In practice, it is very possible that multiple moving targets are closely located. Therefore, (19) should be further modeled into a multicomponent LFM form as

$$s(\tilde{t}_n) = \sum_{k=1}^{K} s_k(\tilde{t}_n) = \sum_{k=1}^{K} A_k \cdot \exp\left[j2\pi f_k^{\,d}\tilde{t}_n + j\pi\gamma_k^{d}\tilde{t}_n^{\,2}\right] \tag{21}$$

where $s_k(\tilde{t}_n)$ is the k-th moving target signal model in LFM form with $f_k^d = f_k^{dc} - f_k^{dt}$ and $\gamma_k^d = \gamma^{dc} - \gamma_k^{dt}$ denoting the Doppler centroid frequency and chirp rate of the k-th LFM component, respectively. In (21), K moving targets are considered, A_k is the amplitude of the k-th LFM component, and f_k^{dt} and γ_k^{dt} are the Doppler frequency shift and chirp rate difference of the k-th moving target, respectively. Furthermore, f_k^{dc} is the k-th target location related Doppler frequency and γ^{dc} is the common chirp rate.

LVD, as a recently developed TF analysis for multicomponent LFM signal, is a natural and true representation for the linear and quadratic parameters, f_k^d and γ_k^d [22]. To compute the LVD representation, a parametric symmetric instantaneous autocorrelation function (PSIAF) is defined as

$$R_s^C(\tau,\tilde{t}_n) = s\left(\tilde{t}_n + \frac{\tau+a}{2}\right)s^*\left(\tilde{t}_n - \frac{\tau+a}{2}\right) \tag{22}$$

where the superscript * indicates conjugate operation, τ is the time-lag variable, and a is a constant time-delay parameter. By substituting (21) into (22), we have

$$\begin{aligned} R_s^C(\tau,\tilde{t}_n) &= \sum_{k=1}^{K} R_{s_k}^C(\tau,\tilde{t}_n) + \sum_{k=1}^{K-1}\sum_{l=k+1}^{K}\left[R_{s_k s_l}^C(\tau,\tilde{t}_n) + R_{s_l s_k}^C(\tau,\tilde{t}_n)\right] \\ &= \sum_{k=1}^{K} A_k^2 \exp\left[j2\pi f_k^d(\tau+a) + j2\pi\gamma_k^d(\tau+a)\tilde{t}_n\right] + \sum_{k=1}^{K-1}\sum_{l=k+1}^{K}\left[R_{s_k s_l}^C(\tau,\tilde{t}_n) + R_{s_l s_k}^C(\tau,\tilde{t}_n)\right] \end{aligned} \tag{23}$$

where $R_{s_k}^C(\tau,\tilde{t}_n)$ and $R_{s_k s_l}^C(\tau,\tilde{t}_n)$ denote the auto-term and cross-term of the PSIAF, respectively. As noted from the exponential phase terms in (23), the resampled slow-time $\tilde{t}_n$ and the time-lag τ are coupled with each other. Such a coupling is the underlying mechanism for the degradation of the LFM signal representation in TF domain. In SAR moving target imaging scenario, this coupling can be referred to a linear Doppler frequency $\gamma_k^d(\tau+a)$ migration along with the resampled slow-time $\tilde{t}_n$. In other words, if $\tilde{t}_n$ is decoupled from τ, each auto-term of PSIAF would become a distinct peak in CFCR domain by using a simple 2-D FT with respect to $\tilde{t}_n$ and τ. Different from the coupling encountered in Section III, where the resampled range wavenumber k_r is coupled with the slow-time t_n, we have used the azimuth resampling of PFA to remove the coupling. Or equivalently, the slow-time variable t_n is resampled into $\tilde{t}_n$ as

$k_r t_n = k_0 \tilde{t}_n$, and the range walk is corrected. In LVD, the coupling between Doppler frequency and resampled slow-time is handled by a scaling scheme, where the scaling operator is generally defined as

$$\Gamma\left[R_s^C\left(\tau,\tilde{t}_n\right)\right] = R_s^C\left(\tau,\frac{\tilde{\tilde{t}}_n}{(\tau+a)h}\right) \tag{24}$$

where $\Gamma[\cdot]$ denotes the scaling operator, $\tilde{\tilde{t}}_n$ indicates the scaled slow-time variable and h is the scaling factor. Substituting (23) into (24), the scaled PSIAF yields

$$\begin{aligned}&\Gamma\left[R_s^C\left(\tau,\tilde{t}_n\right)\right]\\&=\sum_{k=1}^{K}A_k^2\exp\left[j2\pi f_k^d(\tau+a)+j2\pi\frac{\gamma_k^d}{h}\tilde{\tilde{t}}_n\right]+\sum_{k=1}^{K-1}\sum_{l=k+1}^{K}\left[R_{s_k s_l}^C\left(\tau,\frac{\tilde{\tilde{t}}_n}{(\tau+a)h}\right)+R_{s_l s_k}^C\left(\tau,\frac{\tilde{\tilde{t}}_n}{(\tau+a)h}\right)\right].\end{aligned} \tag{25}$$

From (25), it can be found that the coupling in the PSIAF of LVD has been removed for K auto-terms. By applying FT operations to both τ and $\tilde{\tilde{t}}_n$, the LVD representation can be therefore obtained as

$$\mathcal{L}_s\left(\hat{f}^d,\hat{\gamma}^d\right)=\mathcal{F}_{\tilde{\tilde{t}}_n}\left\{\mathcal{F}_\tau\left\{\Gamma\left[R_s^C\left(\tau,\tilde{t}_n\right)\right]\right\}\right\}=\sum_{k=1}^{K}\mathcal{L}_{s_k}\left(\hat{f}^d,\hat{\gamma}^d\right)+\sum_{k=1}^{K-1}\sum_{l=k+1}^{K}\mathcal{L}_{s_k s_l}\left(\hat{f}^d,\hat{\gamma}^d\right) \tag{26}$$

where $\mathcal{F}_\tau$ and $\mathcal{F}_{\tilde{\tilde{t}}_n}$ denote the FT operations to the time-lag τ and scaled slow-time $\tilde{\tilde{t}}_n$, respectively. In (26), $\mathcal{L}_{s_k}\left(\hat{f}^d,\hat{\gamma}^d\right)$ is one of the auto-terms of the LVD representation, which can be analytically derived as

$$\mathcal{L}_{s_k}\left(\hat{f}^d,\hat{\gamma}^d\right)=A_k^2\exp\left(j2\pi a f_k^d\right)\delta\left(\hat{f}^d-f_k^d\right)\delta\left(\hat{\gamma}^d-\gamma_k^d/h\right) \tag{27}$$

where $\delta(\cdot)$ denotes the Dirac delta function. As noted in (26)-(27), for the k-th moving target, the Doppler parameters, f_k^d and γ_k^d, can be represented by the auto-term of LVD in the CFCR domain $\left(\hat{f}^d,\hat{\gamma}^d\right)$ with the coordinates $\left(f_k^d,\gamma_k^d/h\right)$. Obviously, the scaling factor h introduces a scaled axis for the representation of the Doppler chirp rate. To directly read the chirp rate from the CFCR plane, h should be equal to one. Next, to determine the constant time-delay a, the scaling operator in (24) can be referred as $(h\tau+ah)\tilde{t}_n=\tilde{\tilde{t}}_n$. According to the analysis in [22], ah is required to be one for a desirable accuracy in the implementation

of the scaling operator. Thus, the optimal value of a should also equal to one. Therefore, in the generation of PSIAF, the constant time-delay a, apart from the regular time-lag variable τ, is required to be 1 second. For infinite-length continuous LFM signal, when a=1s and h=1, the scaling operator achieves optimal performance in terms of accuracy [22]. In such a case, the optimal kernel for the scaling operation obeys Keystone principle [22], which can justify the above analysis that LVD is capable of correcting the linear Doppler frequency migration.

In (26), the sum of $\mathcal{L}_{s_k s_l}\left(\hat{f}^d,\hat{\gamma}^d\right)$ includes all the cross-terms of the LVD representation that may interfere the representation of the auto-terms. Due to the space limitation, we do not give details about the derivation of the cross-terms which can be referred to Lemma 2 in [22]. It has been theoretically concluded in [22] that for infinite-length continuous LFM setting, when the parameters a and h are both set to one, the modulus of the LVD representation will tend to be

$$\left|\mathcal{L}_s\left(\hat{f}^d,\hat{\gamma}^d\right)\right| \to \sum_{k=1}^{K}|A_k|^2\,\delta\left(\hat{f}^d - f_k^d\right)\delta\left(\hat{\gamma}^d - \gamma_k^d\right) \tag{28}$$

where the cross-terms have negligible magnitude compared with that of the auto-terms.

However, in practice, the azimuth phase data have a finite length in a discrete form. Supposing ΔT is the PRI, we use $s(n\Delta T)$ to denote the discrete form of $s(\tilde{t}_n)$ in (21), where $1 \le n \le N_a$ is the sample index, N_a is the total number of samples and $T_a = N_a\Delta T$. If the number of samples for PSIAF is assumed to be N, to guarantee a can be approximately set to 1s, T_a should satisfy $N_a\Delta T \ge N\Delta T + 1$. Or equivalently, T_a is required to be large enough to guarantee at least 1s time redundancy. Also, due to the finite signal length, the magnitude of the cross-terms may not be negligible. Fortunately, the LVD still maintains asymptotic linearity (Theorem 2-P1, [22]), which concludes that the longer signal length or CPI T_a is, the lower magnitudes of the cross-terms (relative to the auto-terms) are. Moreover, as the linear Doppler frequency migration has been corrected by the Keystone scaling process in LVD, a coherent integral can be fully achieved by FT to highly concentrate the energy of the auto-terms. Thus, a significantly high ratio between the auto-terms and cross-terms can be achieved. For finite-discrete signal, the ideal Dirac delta function

used in the formulation of the LVD representation in (28) will be degraded into a sinc function. This results in resolution limitation on the representation of the Doppler parameters [22]. The resolutions, defined as -3dB width of main-lobe of the sinc function, are analytically derived as $\rho_{f^d} = 1/T_a$ and $\rho_{\gamma^d} = 2/T_a$ (Theorem 3-P6, [22]) for the Doppler centroid frequency and chirp rate, respectively. The two resolution expressions imply that the longer CPI is, the higher resolution can be achieved in the LVD representation.

From the analysis above, a large CPI is preferred for an accurate LVD representation in terms of representative resolution and magnitude ratio between the auto-terms and cross-terms. However, in real moving target scenario, it would be impractical to assume the target velocity is constant during a large CPI. High order target movement should be considered which may cause the target signal model deviates from the LFM form. Therefore, the selection of CPI should be a tradeoff between the accuracy and complexity. Discussions of imaging the target with non-constant velocity will be provided in Section V.C. Finally, an intuitive illustration for computation of the LVD representation is depicted in Fig. 2.

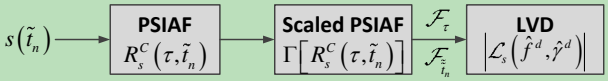

Fig. 2. LVD computation flowchart.

C. SAR Moving Target Imaging Algorithm

When we apply LVD for SAR moving target representation, it should be aware that in the scenario of multiple moving targets, there will be multiple peaks on the Doppler CFCR plane. Therefore, it is necessary to identify a specific peak with respect to its corresponding moving target in the SAR image. To this end, the interferometric phase, Ψ_{in}, as expressed in (17), can be utilized as an auxiliary information for the identification. The interferometric phase can be retrieved by three-channel clutter suppressed interferometry (CSI) [14] or two-channel along-track interferometry (ATI) [13]. According to theoretical and experimental analysis in [14], CSI outperforms ATI in terms of accuracy. Thus, CSI is used to obtain the interferometric phase and further estimate the radial velocity and geo-located position of each target as $\hat{v}_r(l)$ and $\hat{x}(l)$, respectively, where $l = 1,2,\cdots K$ indicates the detected moving target ID. The identification procedure of multiple moving targets from the LVD representation is given in Table 1.

Table 1. Identification procedure for multiple moving targets.

i). The k-th moving target is represented by LVD at $\left(f_k^d, \gamma_k^d\right)$ on the Doppler CFCR plane;

ii). Substitute each estimate $\hat{v}_r(l)$ into f_k^d to obtain another target geo-located estimate $\hat{x}'(l)$;

iii). If $\left|\hat{x}'(l) - \hat{x}(l)\right| \le \eta$ (η is a small value), the k-th target can be identified as the l-th moving target in the SAR image, and then switch to **iv**), else, $l = l + 1$ and switch to **ii**);

iv). While $k \le K$, set $l = 1$ and $k = k + 1$, and switch to **i**); else, stop the procedure.

At this point, we summarize our proposed SAR-GMTIm algorithm into a flowchart as shown in Fig. 3. Firstly, multichannel SAR is employed for receiving the echo signal. Then, PFA is used to form the SAR image with the data from each channel, where stationary scene can be fully focused but moving target would be still defocused and displaced. Next, DPCA is applied for the clutter suppression, and moving target detection is performed in the clutter-suppressed SAR image domain. LVD, as depicted in Fig. 2, proceeds to represent the detected moving targets on the Doppler CFCR domain. By utilizing the interferometric phase, multiple moving targets can be identified from the LVD representation by using the procedures in Table 1. Based on the LVD representation with respect to each moving target, the moving target velocity can be estimated according to the relationships formulated in (20), and the moving target image can be geo-located and refocused by matched-filtering.

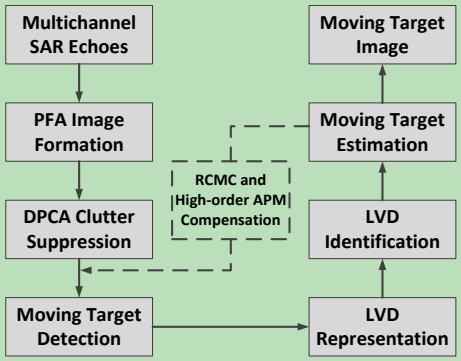

Fig. 3. Flowchart of the proposed SAR-GMTIm algorithm.

As noted in Fig. 3, we perform the moving target detection in the clutter-suppressed SAR image domain. However, the target movement leads to both APM and RCM in the SAR echo signal, which will result in azimuth and range smearing, respectively. Especially in the scenario of highly maneuvering target and/or small moving target with reduced radar cross section (RCS), although the clutter suppression has been

performed, the severe smearing will decrease the effective target SCNR, which may degrade the performance of the moving target detection badly. Also, the RCM itself would degrade the accuracy of the LVD representation. To this end, we design RCMC and high-order APM compensation to enhance the target SCNR in an iterative manner. More specifically, in Fig. 3, we iteratively perform the moving target detection, LVD representation, moving target estimation and RCMC and high-order APM compensation. During the iteration, the possible RCM can be gradually corrected to achieve the best accuracy of the LVD representation. Furthermore, a certain extent of removing the smearing in both range and azimuth can improve the performance of the moving target detection.

V. DISCUSSIONS

In this section, to enhance the applicability of the proposed algorithm, some practical issues, including uncompensated SAR motion error, imaging of fast moving target, maneuvering target and small/weak target, will be discussed.

A. Uncompensated SAR Motion Error

In (14), the last phase term, $k_r \Delta R\left(-k_x \mathrm{R}_0 / k_r v\right)$, denotes the phase term induced by the uncompensated SAR motion error $\Delta R(\cdot)$ in post-PFA data domain. One convenient approximation of Taylor series expansion up to first order at $k_r = k_0$ yields

$$k_r \Delta R\left(-\frac{k_x}{k_r}\frac{\mathrm{R}_0}{v}\right) \approx k_0 \Delta R\left(-\frac{k_x}{k_0}\frac{\mathrm{R}_0}{v}\right) + \left[\Delta R\left(-\frac{k_x}{k_0}\frac{\mathrm{R}_0}{v}\right) + \frac{k_x}{k_0}\frac{\mathrm{R}_0}{v}\Delta R'\left(-\frac{k_x}{k_0}\frac{\mathrm{R}_0}{v}\right)\right]\left(k_r - k_0\right) \tag{29}$$

where $\Delta R'(\cdot)$ indicates derivative of $\Delta R(\cdot)$. Using a variable substitution of $\tilde{t}_n = -k_x \mathrm{R}_0 / k_0 v$, (29) can be explicitly shown as

$$k_r \Delta R\left(-k_x \mathrm{R}_0 / k_r v\right) = \underbrace{k_0 \Delta R\left(\tilde{t}_n\right)}_{\text{Phase error}} + \underbrace{\left[\Delta R\left(\tilde{t}_n\right) - \tilde{t}_n \Delta R'\left(\tilde{t}_n\right)\right]\left(k_r - k_0\right)}_{\text{RCM error}} . \tag{30}$$

The first term in (30), which is the error $\Delta R\left(\tilde{t}_n\right)$ multiplied with constant k_0, is known as an azimuth phase error. The residual terms have been modeled as linear relation with $\Delta k_r = k_r - k_0$, which may result in an

RCM error that is in accordance with $\Delta R(\tilde{t}_n) - \tilde{t}_n \Delta R'(\tilde{t}_n)$. To obtain a high quality target image, both the phase and RCM errors should be compensated. In [27], a data-driven motion error compensation approach is presented, which is capable of first estimating the phase error, and then calculating the RCM error based on (30). Referring to the variable substitution $\tilde{t}_n = -k_x \mathrm{R}_0 / k_0 v$, it is also known as the resampled slow-time variable introduced in Section III, which in turn validates our previous analysis.

B. Fast Moving Target Imaging

In previous sections, one common assumption employed for the analysis is that the target movement during CPI does not exceed the range resolution cell. In such a case, the target range walk can be corrected by PFA for each channel SAR image formation. However, this assumption may not be valid for fast moving target. Due to the large radial velocity of the target, excessive range walk may exist even after PFA, and simultaneously, the target Doppler shift may exceed the system pulse repetition frequency (PRF), which may accordingly result in Doppler centroid frequency ambiguity. From (20), the target Doppler shift is given as $f^{dt} = 2(r + \mathrm{R}_0) v_r / \lambda \mathrm{R}_0$. If v_r is large, f^{dt} may exceed $\pm$PRF/2, and the Doppler frequency would be folded. By modelling the Doppler shift as $f^{dt} = f^{dt0} + m \cdot \mathrm{PRF}$, where f^{dt0} is the folded Doppler frequency within [-PRF/2, PRF/2] and m is the PRF folding number (integer), for the reference channel, the phase of fast moving target after PFA can be derived as

$$\Psi_0^{\mathrm{RECT}} = -k_x x - k_r r - k_0 \frac{(r + R_0) v_{r0}}{R_0} \tilde{t}_n \underbrace{-2\pi \frac{\Delta k_r}{k_0} (m \cdot \mathrm{PRF}) \tilde{t}_n}_{\text{Excessive range walk}} - k_0 \frac{(v - v_x)^2 + v_r^2}{2R_0} \tilde{t}_n^2 + k_0 \frac{v^2}{2R_0} \tilde{t}_n^2 \qquad (31)$$

where v_{r0} is the folded component of the target radial velocity. Comparing (31) with (15), an excessive range walk can be observed, which is evaluated in terms of the folding number m.

To determine the folding number for multiple moving targets, a simple and effective approach introduced in [5] can be adopted. The image response of each moving target is firstly detected and spotlighted in the clutter-suppressed SAR image domain. Due to the range walk caused by fast moving target, the target image will also be defocused in range dimension. Then, a series of hypotheses for the folding number are set to correct the excessive range walk as modeled in (31), and the target image is

formed by a simple azimuth FT. Next, we can search and find the number m that can achieve the target image with the minimum range defocusing due to the excessive range walk. Entropy [28] of the target image can be used to quantitatively evaluate the focusing quality. Finally, by iterating the above procedure for all detected moving targets, the folding number of each target can be determined. After the determination of m, the range walk can be corrected, and also, the target unfolded Doppler frequency shift f^{dt} can be retrieved according to f^{dt0} obtained from the LVD representation. The unfolded target cross-track velocity v_r can be estimated accordingly.

Remark: Along with the Doppler centroid frequency ambiguity as discussed above, Doppler spectrum may also be ambiguous and folded back into the main Doppler bandwidth [-PRF/2, PRF/2]. Due to the Doppler bandwidth (spectrum) ambiguity, the target truth as well as its ambiguities will appear in the SAR image. Both the target truth and the ambiguous targets will be represented by LVD. To resolve this, multichannel beam-forming technique would be a possible solution [29]-[30]. To incorporate the beam-former into our proposed algorithm, additional SAR channels are required to provide sufficient degrees of freedom.

C. Maneuvering Target Imaging

During the above analysis, we mainly analyze the moving target with constant velocity. For more complicated scenario, where maneuvering targets with non-constant velocity are encountered, the target range curvature and even high-order RCM would be first necessary to be dealt with. To accommodate this, we have designed the specific RCMC in the proposed SAR-GMTIm processing chain as shown in Fig. 3. The RCMC is accomplished based on the moving target estimation in an iterative manner. Although the estimation may not be accurate enough due to the influence of RCM on the LVD representation, the accuracy can be improved gradually followed by RCMC.

For maneuvering target imaging, we model the target trajectory as

$$\mathbf{r}_t\left(t_n\right)=\mathbf{r}_0+\mathbf{R}_0+\mathbf{v}_t t_n+\frac{1}{2}\mathbf{a}_t t_n^{\ 2}+\frac{1}{6}\mathbf{a}_t^{'} t_n^{\ 3} \tag{32}$$

where $\mathbf{a}_t = a_x\vec{\mathbf{x}} + a_r\vec{\mathbf{r}}$ is the target acceleration, and a_x and a_r are the along-track and cross-track components of $\mathbf{a}_t$, respectively. Also, in (32), time derivative of the target acceleration $\mathbf{a}_t^{'} = a_x^{'}\vec{\mathbf{x}} + a_r^{'}\vec{\mathbf{r}}$ is considered, and $a_x^{'}$ and $a_r^{'}$ are the along-track and cross-track components of $\mathbf{a}_t^{'}$, respectively. Higher order acceleration terms are assumed to be negligible in (32). Following similar analysis throughout Sections II-III, after PFA and DPCA, the range-compressed signal of the maneuvering target up to third order phase modulation can be shown as

$$s(\tilde{t}_n) = A \cdot \exp\left[j2\pi\left(f^{dc} - f^{dt}\right)\tilde{t}_n + j\pi\left(\gamma^{dc} - \gamma^{dt}\right)\tilde{t}_n^{\,2} + j\frac{\pi}{3}\left(\gamma^{'dc} - \gamma^{'dt}\right)\tilde{t}_n^{\,3} \right] \tag{33}$$

where

$$\gamma^{dt} = \frac{2\left(v - v_x\right)^2 + 2v_r^{\,2}}{\lambda \mathrm{R}_0} + \frac{2\left(r + R_0\right)a_r}{\lambda R_0}, \quad \gamma^{'dc} = 0, \quad \gamma^{'dt} = \frac{2\left(v - v_x\right)a_x + 2v_r a_r}{\lambda \mathrm{R}_0} + \frac{2\left(r + R_0\right)a_r^{'}}{\lambda R_0} \ . \tag{34}$$

Other parameters can refer to (20). Comparing (33)-(34) with the LFM model under the assumption of constant target velocity as shown in (19)-(20), a cubic phase, mainly due to the target acceleration a_x and time varying acceleration $a_r^{'}$, is introduced. The cubic phase will result in the moving target response with asymmetric sidelobes and decreased energy of main-lobe [23]. Besides, the Doppler chirp rate γ^{dt} in (34) is different from that in (19), where an additional quadratic modulation related with the target radial acceleration a_r can be found.

Prior to achieving the maneuvering target image, LVD is adopted to represent the azimuth signal of the target. In presence of the cubic phase, severe degradation in the LVD representation will occur, since LVD is originally designed for LFM signal representation. As it is well-known that a quadratic phase modulated (or LFM) signal represents itself as a skewed line in TF plane, the line variation indicates the instantaneous frequency (IF) variation of the signal, and the line slope stands for the chirp rate. Analogous to this fact, the signal in (33) with an additive cubic phase will represent itself in TF plane as a skewed parabola. LVD, essentially, is an operator that removes the linear slope of the LFM signal and further cumulates the de-skewed linear distribution into a distinct peak on the final CFCR plane. Thus, when we apply LVD to the

signal with additive cubic phase, it may not be able to concentrate the entire parabola distribution into a single pixel on the CFCR plane, which results in defocusing along both the two axes of CFCR. Therefore, due to the defocusing on the target parametric plane of Doppler CFCR, it will be difficult to extract a distinct peak for representing the target Doppler frequency modulation. Furthermore, the inaccurate representative Doppler parameters cannot be used to fully match the target signal modulation, which will result in residual defocusing.

To compensate the problematic cubic phase, we mainly follow the study in [31]-[32], where it suggests making use of pseudo-WVD (PWVD) to obtain the IF history of the maneuvering target in the TF domain. By integrating the IF history, we can achieve the total instantaneous phase. A third-order polynomial fitting can be therefore utilized to access the significant cubic phase. When the cubic phase is compensated, we can continue to use LVD for moving target representation and further refocus the target image.

Although for maneuvering target imaging, we can adopt the method introduced in [31] to compensate the cubic phase and further obtain a refocused target image based on the LVD representation, it should be noted that both the target along-track velocity v_x and cross-track acceleration a_r will result in a Doppler rate difference. Therefore, it would be difficult to decouple the two effects from the LVD representative Doppler chirp rate. It is still a challenging problem to estimate the target velocity when the target is accelerating. Interested readers can refer to [26], [31]-[32] for a possible solution.

D. Small/Weak Moving Target Imaging

When the moving target is small/weak in RCS, the target SCNR would be low in the echo signal. Although we have performed the clutter suppression to enhance the target SCNR, residual clutter and noise would still degrade the target SCNR especially when the target signal is weak. Detection of the moving target with reduced RCS has been discussed in Section IV.C. In this sub-section, we mainly focus on analysis of performance of the proposed algorithm in small/weak moving target scenario. Firstly, to detect the LVD representation of small/weak target on the Doppler CFCR plane in presence of residual clutter and noise, the output SNR of the LVD representation is a key parameter to be discussed. Higher output SNR leads to a better performance in detecting the target representation. According to the analysis in [22]

(Corollary 1), the LVD is superior to RWT in terms of output SNR, where the output SNR of RWT has a 3dB loss due to its bi-linearity, however, the SNR loss of LVD is less than 3dB because of its asymptotic linearity.

Secondly, due to the low SCNR of moving target, the LVD representative Doppler parameters (f,γ) may be displaced to $(f+\delta f,\gamma+\delta\gamma)$, where δf and $\delta\gamma$ denote the representation errors for the Doppler centroid frequency and chirp rate, respectively. Similar to the perturbation analysis for WHT in [19], the representation errors of LVD have been derived (Theorem 5) in [22]. According to this, we can further derive the estimation accuracies for radial velocity v_r and along-track velocity v_x are bounded as

$$\sigma_{v_r}^2 < \frac{\lambda^2\left(147N^3+36q^2N^2\right)}{4\pi^2\left(98N^4+72q^4\right)\mathrm{SCNR}_{\mathrm{in}}} \quad \text{and} \quad \sigma_{v_x}^2 < \frac{\lambda \mathrm{R}_0}{2}\sqrt{\frac{294h^2}{\pi^2\mathrm{SCNR}_{\mathrm{in}}N}}\ , \tag{35}$$

respectively. In (35), $\mathrm{SCNR}_{\mathrm{in}}$ denotes the input SCNR, and q satisfies $a=q\Delta T$, and $\sigma_{v_r}^2$ and $\sigma_{v_x}^2$ indicate the estimation variances for radial and along-track velocities, respectively. As noted in (35), it is clear that both the estimation variances are inversely proportional to the input SCNR. Lower variance leads to higher representation accuracy.

VI. EXPERIMENTS

In this section, a series of experiments are designed and carried out to examine our presented moving target signatures and evaluate the proposed SAR-GMTIm algorithm based on the LVD representation. Both point target simulation and multichannel raw SAR data are used for the verification.

A. Point Target Simulation

The SAR sensor used for the point target simulation is supposed to be an X-band radar with carrier frequency of 9.75GHz, bandwidth of 75MHz and PRF of 1000Hz. The radar antenna is a linear array of three elements (I =3), where the middle one is the transmitter and all are receivers. The spacing between the two adjacent elements is 0.3m. The aircraft flies with a constant velocity 150m/s at an altitude 6km. The CPI for each moving target imaging is ~2s. The observing scene has the nearest range ~10km from the

radar flight track to the scene center, wherein 8 moving targets (MT1-MT8) and 2 stationary targets (ST1-ST2) are simulated within the scene. All the simulated targets are supposed to be isotropic point-like targets. The simulated target ground truth is shown in Fig. 4, where the 8 moving targets' velocities are given in Table 2 with along-track (azimuth) velocity v_x and radial (slant-range) velocity v_r. Both clutter and noise are simulated in each channel echo signal, which are both supposed in homogeneous Gaussian distribution. By using PFA for the SAR image formation of each channel, we measure the input SCNR of each channel SAR image -5.51dB. After DPCA is applied for the clutter suppression, the input SCNR can be improved to 9.72dB in the clutter-suppressed SAR image.

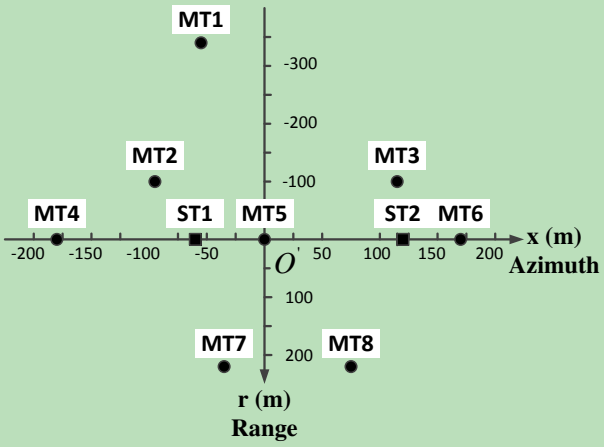

Fig. 4. Simulated target ground truth.

From the SAR parameters provided above, the SAR image can be formed in 2m spatial resolution. Thus, PFA allows the generation of a SAR image with a size of ~3km in diameter [23]. It is large enough to cover the simulated target scene in Fig. 4. After the clutter suppression, LVD is applied in range-compressed data domain to represent the moving targets on the Doppler CFCR plane. For maneuvering target, additional processing would be required to compensate the possible RCM and high-order APM as shown in Fig. 3. Next, under the LVD representation, the moving targets' velocities are estimated and shown in Table 2 as the along-track and radial estimations $\hat{v}_x$ and $\hat{v}_r$. The PRF folding number m is also estimated to incorporate fast moving target.

Table 2. Simulated and estimated target velocities.

	v_x (m/s)	v_r (m/s)	$\hat{v}_x$ (m/s)	$\hat{v}_r$ (m/s)	m
MT1	-2.0	30.0	-1.93	30.91	2
MT2	21.0	1.3	21.21	1.20	0
MT3	-15.0	17.0	-15.28	17.02	1
MT4	-2.1	-1.1	-2.08	-1.06	0
MT5	1.1	-1.0	1.11	-0.99	0
MT6	2.2	-1.2	2.25	-1.16	0
MT7	-2.2	-22.0	-2.24	-21.60	-1
MT8	2.1	-21.0	2.19	-20.59	-1

Based on the LVD representation, the result of SAR moving target imaging is given in Fig. 5. The magnitude of the SAR image is evaluated in dB. Each circle in Fig. 5 indicates the target ground truth. Due to the target movement, the moving target response is displaced and defocused as indicated by square symbol. Referring to the simulated target velocities in Table 2, large target along-track velocity leads heavy smearing in azimuth, e.g., MT2 and MT3, and large target radial velocity results in range defocusing, e.g., MT1, MT3, MT7 and MT8. In addition, MT4-MT6 are slow moving targets located within the same range cell, where 2 additional stationary targets ST1-ST2 are also in the range cell. After the processing of the proposed algorithm, each target is geo-located (re-located) and refocused as indicated by the cross symbol.

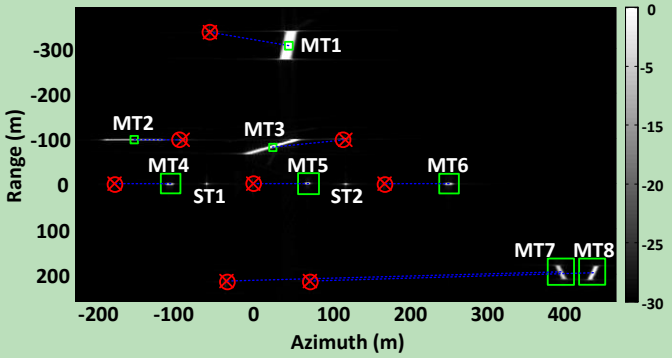

Fig. 5. SAR moving target imaging result (Circle: moving target ground truth; Square: displaced and defocused moving target; Cross: geo-located and refocused moving target by the proposed algorithm).

Fig. 6(a)-(c) illustrate TFR for moving targets MT4-MT6 by LVD, RWT and FrFT, respectively. For the LVD representation in Fig. 6(a), each moving target is represented as a distinct peak in the CFCR domain, and the representative coordinates are read as the Doppler centroid frequency and chirp rate. Fig. 6(b) shows the RWT representation. Due to its bi-linearity, both auto-terms and cross-terms are observed in the

parametric domain of radial coordinate and rotational angle. Furthermore, the location of the representative auto-term for MT5 is too close to the cross-term from MT4 and MT6, which becomes a serious consequence in acquisition of the auto-term coordinates of MT5. Fig. 6(c) shows the FrFT representation, where there is no cross-term because of its linearity. However, in the FrFT representation, the absolutely dynamic range of the magnitude is smaller than those of LVD and RWT [22]. Therefore, relatively high side-lobes of the representative peak of FrFT may interfere the acquisition of the coordinates.

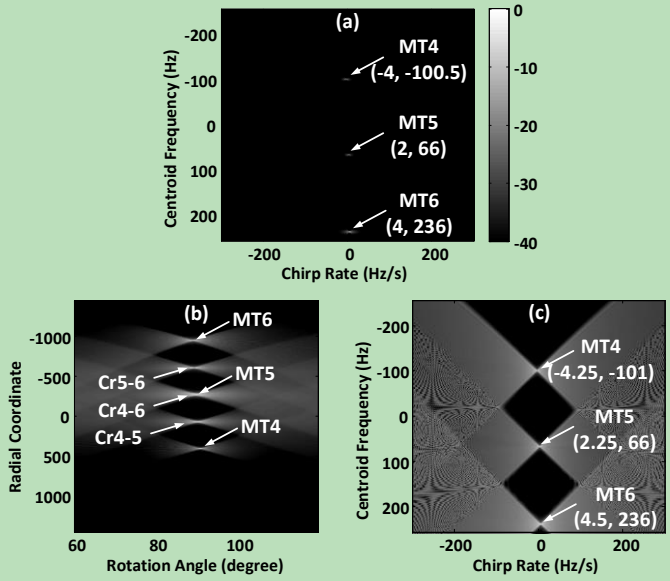

Fig. 6. TFR for MT4-MT6 by (a) LVD, (b) RWT and (c) FrFT, respectively (RWT is with rotational angle searching step 0.1° [18], and FrFT is with rotational order searching step 0.0002 [21]).

To show the imaging performance of the LVD and FrFT-based methods, Fig. 7(a)-(c) gives the defocused and refocused azimuth responses of MT4-MT6, respectively. The Doppler parameters used for the target refocusing can be read from Fig. 6(a) and (c) for the representation of LVD and FrFT, respectively. A common phenomenon observed throughout Fig. 7(a)-(c) is that the defocused target responses (dotted lines) have widened main-lobes and high side-lobes. The refocused target responses based on the FrFT representation (dashed lines) have narrower main-lobes and lower side-lobes, which indicates a better focusing quality. Those based on the LVD representation (solid lines) have the most narrow main-lobes and lowest side-lobes, which indicates the best focusing quality.

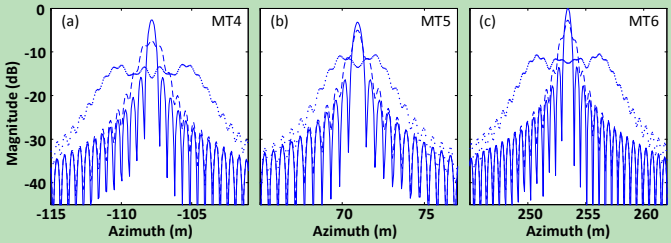

Fig. 7. Azimuth responses of defocused and refocused (a) MT4, (b) MT5 and (c) MT6 (dotted line: defocused target response; dashed line: refocused target response based on FrFT representation; solid line: refocused target response based on LVD representation).

The proposed algorithm also has the capability to image fast moving target. As mentioned in Section V.B, the large target radial velocity may result in excessive range walk. For instance, in Fig. 5, MT3 is a fast moving target. Due to the excessive range walk, range defocusing can be observed, which may degrade the LVD representation for the moving target. By correcting the range walk using the approach introduced in [5], the range defocusing can be removed as the contour image shown in Fig. 8(a). Then, according to the LVD representation for MT3, the target contour image can be refocused as shown in Fig. 8(b), where a highly focused SAR moving target image can be achieved.

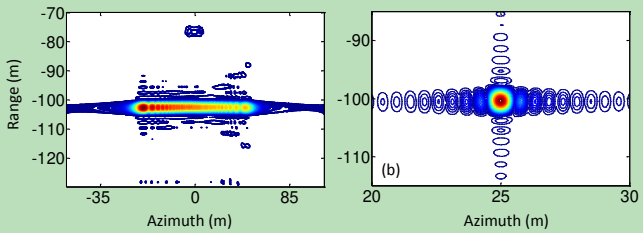

Fig. 8. MT3 contour image ((a): range focused image after range walk correction; (b): final focused image).

B. Raw Data Experiment

The raw SAR data were collected by an X-band radar with three channels. The transmitted pulse bandwidth is 18MHz, PRF is ~830Hz, and transmitting antenna beam-width is 4.5°. The airborne platform velocity is ~100m/s and the nearest range to the observing scene center is ~60km. The synthetic aperture time duration is ~47s, and the total acquisition time for the collected data is ~19s. The CPI used for the SAR moving target imaging is ~2.47s, which is the middle section of the collected data. At first, we apply

PFA for SAR image formation of each channel data. Also, the uncompensated SAR motion error is compensated according to the discussion in Section V.A. Next, for the clutter suppression, advanced hybrid DPCA/ATI [14] is applied to incorporate the possible nonhomogeneous clutter in real scene. Followed by the proposed SAR-GMTIm algorithm as depicted in Fig. 3, the processing result is shown in Fig. 9. As seen from the SAR image, the observing scene contains a highway where the moving targets may have large velocities on the road. In total, 14 moving targets are geo-located and imaged by the proposed algorithm. Each moving target is marked at its geo-located position by square symbols. For an intuitive display, the estimated target velocity is indicated by the squared color whose indicative velocity can refer to the color bar at right side of the figure. As noted in Fig. 9, all the fast moving targets are geo-located on the high-way, except one slow moving target marked as MT11, which is geo-located at a rural road. For MT11, the estimated PRF folding number is 0, and the target radial and along-track velocities are estimated to be 5.65m/s and 3.76m/s, respectively.

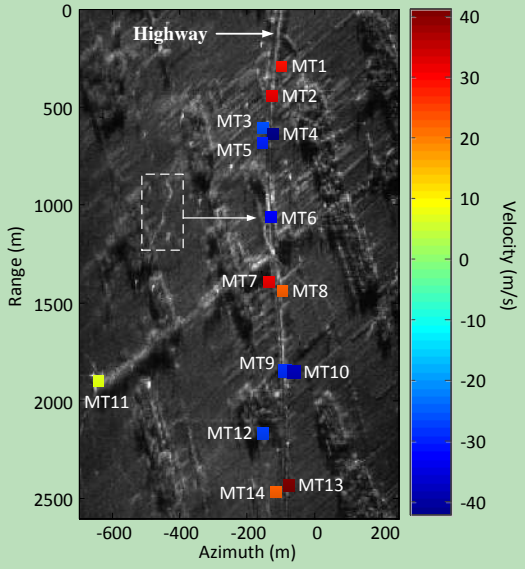

Fig. 9. Multichannel raw SAR data imaging result.

Considering MT6 as indicated by the dashed box in Fig. 9, due to the target movement, its response is both displaced and defocused. In adoption of the proposed algorithm, the target's PRF folding number is estimated to be -2, and the target radial and along-track velocities are estimated to be -22.31m/s and 23.96m/s, respectively. As seen in Fig. 10(a), the target image is given in the clutter-suppressed SAR image

domain, where range defocusing is obvious due to the target fast movement. According to Section V.B, the target excessive range walk is corrected, and the range defocusing is removed as seen in Fig. 10(b), where the target azimuth defocusing still exists. Next, based on the LVD representation, the fully focused target image is obtained in Fig. 10(c). Entropy value [28] is provided for each SAR image to give a quantitative evaluation for the target focusing quality. The smaller the entropy the better the image focuses.

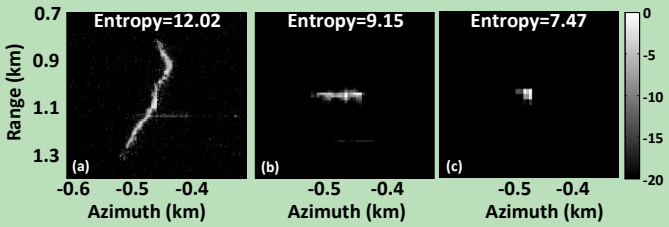

Fig. 10. MT6 SAR image ((a)-(c): defocused, range refocused and azimuth refocused images, respectively).

In Fig. 9, the moving targets, MT9 and MT10, are closely located. In the experiment, both targets are estimated to have the same PRF folding number of -2. The LVD and FrFT representations are given in Fig. 11(a) and (b), respectively, where the representative Doppler parameters of each target are labeled. As seen from Fig. 11(a), LVD is capable of representing the two moving targets distinctly on the Doppler CFCR plane. However, high side-lobes around the representative peaks can be observed in the FrFT representation in Fig. 11(b).

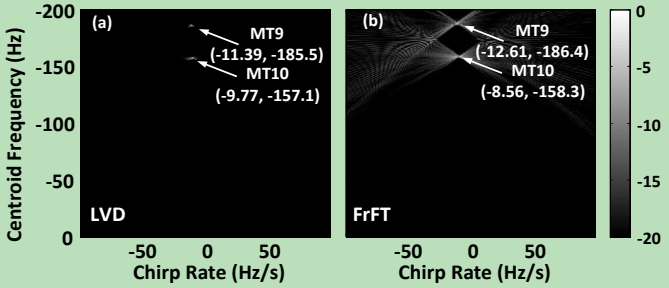

Fig. 11. TFR for MT9-MT10 by (a) LVD and (b) FrFT, respectively.

By reading the coordinates of each representative peak in the CFCR domain of LVD (Fig. 11(a)) and FrFT (Fig. 11(b)), each target image is refocused as shown in Fig. 12. Fig. 12(a)-(c) illustrate the defocused, FrFT and LVD refocused SAR images of MT9, respectively. It is noted that the LVD representation has the

superior performance on the target focusing compared with that of FrFT, where better focused SAR image with smaller entropy can be obtained by our proposed SAR-GMTIm algorithm based on LVD. Fig. 12(d)-(f) give the defocused, FrFT and LVD refocused SAR images of MT10, respectively. Entropy of the target image focused under the LVD representation is also smaller than that achieved under the FrFT representation. Finally, the total computation time for the proposed algorithm based on the LVD representation and that based on the FrFT representation are 6min05s and 6min41s, respectively. An HP desktop computer with Intel Core i7 3.4GHz CPU, 24GB RAM and Matlab 7.12.0 is used for the computation.

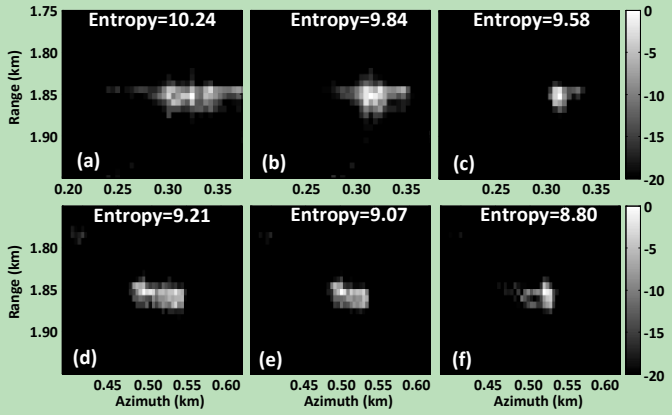

Fig. 12. MT9 and MT10 SAR images ((a)-(c): defocused, FrFT and LVD refocused images of MT9, respectively; (d)-(e): defocused, FrFT and LVD refocused images of MT10, respectively).

VII. CONCLUSIONS

In this paper, a generic SAR moving target signature is thoroughly analyzed, and a new SAR-GMTIm algorithm is proposed based on the novel LVD representation. The proposed algorithm has superior capability to image multiple moving targets even when they are closely located at the same range cell. Practical issues, including uncompensated SAR motion error and imaging of maneuvering target and small/weak target, are also discussed. In summary, our proposed algorithm exploits the Keystone principle twice. The first one is in the SAR image formation by PFA. Because the azimuth resampling of PFA has the inherently same mechanism as KT, the linear coupling between range frequency and azimuth slow-time is removed for both stationary and moving target, simultaneously. The second one is in the LVD

representation. The Keystone principle is adopted as the optimal kernel for the scaling operation in LVD so that the target linear coupling between the Doppler frequency and resampled azimuth slow-time is removed. Both point target simulation and raw SAR data experiment have verified the proposed SAR-GMTIm algorithm.

ACKNOWLEDGMENT

This project was sponsored by Temasek Laboratories @ NTU.

REFERENCES

[1] R. K. Raney, "Synthetic aperture imaging radar and moving targets," *IEEE Trans. Aerosp. Electron. Syst.*, vol. AES-7, no. 3, pp. 499-505, May. 1971.

[2] J. K. Jao, and A. Yegulalp, "Multichannel synthetic aperture radar signatures and imaging of a moving target," *Inverse Problem*, vol. 29, no. 5, pp. 1-33, 2013.

[3] S. Zhu, G. Liao, Y. Qu, Z. Zhou, and X. Liu, "Ground moving target imaging algorithm for synthetic aperture radar," *IEEE Trans. Geosci. Remot. Sens.*, vol. 49, no. 1, pp. 462-477, Jan. 2011.

[4] G. Gao, and G. Shi, "The CFAR detection of ground moving targets based on a joint metric of SAR interferogram's magnitude and phase," *IEEE Trans. Geosci. Remot. Sens.*, vol. 50, no. 9, pp. 3618-3624, Sep. 2012.

[5] J. Qian, X. Lv, M. Xing, L. Li, and Z. Bao, "Motion parameter estimation of multiple ground fast-moving targets with a three-channel synthetic aperture radar," *IET Radar Sonar Navig.*, vol. 5, no. 5, pp. 582-592, Jun. 2011.

[6] G. Sun, M. Xing, X. Xia, Y. Wu, and Z. Bao, "Robust ground moving-target imaging using deramp-Keystone processing," *IEEE Trans. Geosci. Remot. Sens.*, vol. 51, no. 2, pp. 966-982, Feb. 2013.

[7] R. P. Perry, R. C. DiPietro, and R. Fante, "SAR imaging of moving targets," *IEEE Trans. Aerosp. Electron. Syst.*, vol. 35, no. 1, pp. 188-200, Jan. 1999.

[8] D. Zhu, Y. Li, and Z. Zhu, "A keystone transform without interpolation for SAR ground moving-target imaging," *IEEE Geosci. Remot. Sens. Lett.*, vol. 4, no. 1, pp. 18-22, Jan. 2007.

[9] F. Zhou, R. Wu, M. Xing, and Z. Bao, "Approach for single channel SAR ground moving target imaging and motion parameter estimation," *IET Radar Sonar Navig.*, vol. 1, no. 1, pp. 59-66, Feb. 2007.

[10] G. Li, X. –G. Xia, and Y. –N. Peng, "Doppler Keystone transform: An approach suitable for parallel implementation of SAR moving target imaging," *IEEE Geosci. Remot. Sens. Lett.*, vol. 5, no. 4, pp. 573-577, Oct. 2008.

[11] S. Barbarossa, "Detection and imaging of moving objects with synthetic aperture radar: part 1. Optimal detection and parameter estimation theory," *IEE Proc., Radar Sonar Navig.*, vol. 139, no. 1, pp. 79-88, Feb. 1992.

[12] S. Barbarossa, "Detection and imaging of moving objects with synthetic aperture radar: part 2. Joint time-frequency analysis by Wigner-Ville distribution," *IEE Proc., Radar Sonar Navig.*, vol. 139, no. 1, pp. 89-97, Feb. 1992.

[13] R. W. Deming, "Along-track interferometry for simultaneous SAR and GMTI: application to Gotcha challenge data", *Proc. SPIE*, vol. 8051, pp. 1-18, 2011.

[14] R. W. Deming, S. Maclntosh, M. Best, "Three-channel processing for improved geo-location performance in SAR-based GMTI interferometry," *Proc. SPIE,* vol. 8394, pp. 1-17, 2012.

[15] H. S. C. Wang, "Mainlobe clutter cancellation by DPCA for space-based radars," *in Proc. IEEE Aerosp. Appl. Conf. Dig.*, pp. 1-28, Feb. 1991.

[16] D. Cerutti and I. Sikaneta, "Optimum GMTI processing for space-based SAR/GMTI systems," *in Proc. EUSAR*, pp. 1-4, Jun. 2010.

[17] T. A. C. M. Claasen and W. F. G. Mechlenbräuker, "The Wigner distribution—A tool for time-frequency signal analysis—Part I: Continuous-time signals," *Philips J. Res.*, vol. 35, pp. 217-250, 1980.

[18] J. C. Wood, and D. T. Barry, "Radon transformation of time-frequency distributions for analysis of multicomponent signals," *IEEE Trans. Signal Process.*, vol. 42, no. 11, pp. 3166-3177, Nov. 1994.

[19] S. Barbarossa, "Analysis of multicomponent LFM signals by a combined Wigner-Hough transform," *IEEE Trans. Signal Process.*, vol. 43, no. 6, pp. 1511-1515, Jun. 1995.

[20] M. Wang, A. K. Chan, and C. K. Chui, "Linear frequency-modulated signal detection using Radon-ambiguity transforms," *IEEE Trans. Signal Process.*, vol. 46, no. 3, pp. 571-586, Mar. 1998.

[21] L. B. Almeida, "The fractional Fourier transform and time-frequency representation," *IEEE Trans. Signal Process.*, vol 42, no. 11, pp. 3084-3091, Nov. 1994.

[22] X. Lv, G. Bi, C. Wan, and M. Xing, "Lv's distribution: principle, implementation, properties, and performance," *IEEE Trans. Signal Process.*, vol. 59, no.8, pp. 3576-3591, Aug. 2011.

[23] W. G. Carrara, R. S. Goodman, and R. M. Majewski, "*Spotlight Synthetic Aperture Radar—Signal Processing Algorithms*," Artech House, Norwood, MA, 1995.

[24] G. D. Martin, A. W. Doerry, and M. W. Holzrichter, "A novel polar format algorithm for SAR images utilizing post azimuth transform interpolation," *Sandia Report SAND2005-5510*, Sep. 2005.

[25] L. Zhang, Z. J. Qiao, M. D. Xing, L. Yang and Z. Bao, "A robust motion compensation approach for UAV SAR imagery," *IEEE Trans. Geosci. Remot. Sens.*, vol. 50, no. 8, pp. 3202-3218, Aug. 2012.

[26] M. Xing, X. Jiang, R. Wu, F. Zhou, and Z. Bao, "Motion compensation for UAV SAR based on raw radar data," *IEEE Trans. Geosci. Remot. Sens.*, vol. 47, no. 8, pp. 2870-2883, Aug. 2009.

[27] L. Yang, M. Xing, Y. Wang, L. Zhang, and Z. Bao, "Compensation for the NsRCM and phase error after polar format resampling for airborne spotlight SAR raw data of high resolution," *IEEE Geosci. Remot. Sens. Lett.*, vol. 10, no. 1, pp. 165-169, Jan. 2013.

[28] T. J. Kragh, "Monotonic iterative algorithm for minimum-entropy autofocus," *IEEE Int. Conf. Image Process.*, Atlanta, pp. 645-648, 2006.

[29] N. Gebert, G. Krigeger, and A. Moreira, "Digital beamforming on receive: techniques and optimization strategies for high-resolution wide-swath SAR imaging," *IEEE Trans. Aero. Elec. Sys.*, vol. 45, no. 2, pp.: 564-592, Apr. 2009.

[30] J. Li, P. Stoica and Z. Wang, "Doubly constrained robust Capon beamformer," *IEEE Trans. Signal Process.*, vol. 52, no. 9, pp. 2407-2423, Sep. 2004.

[31] J. J. Sharma, C. H. Gierull, and M. J. Collins, "Compensating the effect of target acceleration in dual-channel SAR-GMTI," *IEE Proc. Radar, Sonar and Navigation*, vol. 153, no. 1, pp.: 53-62, Feb. 2006.

[32] J. J. Sharma, C. H. Gierull, and M. J. Collins, "The influence of target acceleration on velocity estimation in dual-channel SAR-GMTI", *IEEE Trans. Geosci. Remot. Sens.*, vol. 44, no. 1, pp.: 134-147, Jan. 2006.